**RESEARCH ARTICLE**

# Plate corner subduction and rapid localized exhumation: Insights from 3D coupled geodynamic and geomorphological modelling

Alexander Koptev[1,2]  |  Matthias Nettesheim[1]  |  Todd A. Ehlers[1]

[1]Department of Geosciences, University of Tübingen, Tübingen, Germany

[2]GFZ German Research Centre for Geosciences, Potsdam, Germany

**Correspondence**
Alexander Koptev, Department of Geosciences, University of Tübingen, Schnarrenbergstr. 94-96, 72076 Tübingen, Germany.
Email: alexander.koptev@ifg.uni-tuebingen.de; alexander.koptev@gfz-potsdam.de

**Abstract**

Rapid, localized exhumation has been reported at many plate corners between adjacent subduction/collision segments. Here we use a fully-coupled geodynamic and geomorphological modelling approach to investigate overriding plate deformation and resulting rock uplift patterns in these narrow, cuspate regions. In this study, we focus on the effects of internal deformation within a subducting convex-upward-shaped indenter and the strength of the interface between the upper and downgoing plate. The strongest localization of high rock uplift rates in the region above the indenter apex is predicted in experiments with a deformable lower plate, a weak interface layer and lateral shortening accommodated only by subduction (i.e., without an upper plate advance component). Our results suggest that bull's eye shaped structures characterized by young thermochronological ages can, in principle, be reproduced numerically when taking into account a non-rigid subducting plate together with complex brittle-ductile rheology and stratification of the overriding lithosphere and realistically implemented fluvial erosion at its surface.

## 1  |  INTRODUCTION

Plate corners represent narrow, bent segments of the boundary between lithospheric plates (Figure 1a). The transition zones separating the longer, straight to slightly concave zones of plate convergence (subduction or continental collision) are termed as "syntaxial orogens" (Bendick & Ehlers, 2014). Quasi-circular patterns of young thermochronometer ages (also called bull's eye structures) found in the "syntaxial orogens" such as Southeast Alaska (Berger et al., 2008; Enkelmann et al., 2010, 2017; Koons et al., 2010; Falkowski et al., 2014, 2016; Figure 1b), Nanga Parbat and Namche Barwa in the Himalaya (Stewart et al., 2008; Crowley et al., 2009; Enkelmann et al., 2011; Lang et al., 2016; Figure 1c), and the Olympic Mountains in Washington State, USA (Adams & Ehlers, 2017;

Brandon et al., 1998; Michel et al., 2018; Pazzaglia & Brandon, 2001) are indicative of spatially focused rapid rock uplift (>5 mm/year) associated with localized lithospheric deformation in the overriding plate. It is worth noting that this phenomenon may not be restricted to plate corners or even plate boundaries, as rapid neotectonic uplift has also been reported for intracontinental regions of Precambrian cratons (Artyushkov et al., 2018, 2020).

Two conceptual models have been proposed to explain such deformation/rock uplift patterns at the convergent plate corners: (1) a "top-down" model (Figure 1d) referring to a positive feedback between locally enhanced erosion, thermal weakening of the crust, and focused exhumation (Koons et al., 2002, 2013; Zeitler et al., 2001; Zeitler et al., 2014), and (2) a "bottom-up" model (Figure 1e) that considers tectonic processes, specifically the 3D geometry of curved

subducting plates, as the main driver of rapid vertical movements of the surface (Bendick & Ehlers, 2014). In a recent modelling study by Nettesheim et al. (2018), it was shown that the deepest and fastest exhumation occurs in the catchment-scale areas where strong tectonic forcing spatially coincides with a large erosion potential. While the coupled geodynamic/geomorphic models of Nettesheim et al. (2018) reconcile "top-down" and "bottom-up" models, they have a limited ability to reproduce the bull's eye rock uplift structures observed in the "syntaxial orogens" (Bendick & Ehlers, 2014). As demonstrated in a subsequent thermo-mechanical numerical study by Koptev et al. (2019), the curved geometry of the subducting plate appears to be an insufficient condition for the spatial localization of the anomalous exhumation rates. According to their results, an appropriate combination of parameters defining the velocity boundary conditions, the horizontal width of the flexural bulge (indenter) on the subducting plate, and, most importantly, the thermo-rheological structure of the overlying continental lithosphere is also required to concentrate the fast rock uplift within

**Statement of significance**

Our work represents the first successful attempt to reproduce the rapid rock exhumation and associated young thermochronometric ages observed in many plate corners in a fully-coupled numerical experiment, combining state-of-the-art 3D techniques in thermo-mechanical geodynamic and landscape evolution modelling.

isometric or slightly elongated regions with a characteristic diameter of ~100+ km (Koptev et al., 2019).

Here we build upon work by Nettesheim et al. (2018) and Koptev et al. (2019) with thermo-mechanical geodynamic simulations coupled in 3D with landscape evolution model. Our focus is on the influence of the internal deformation in the downgoing plate and the viscosity of the interface layer between the subducting slab and the overriding lithosphere. The modelling approach and experimental
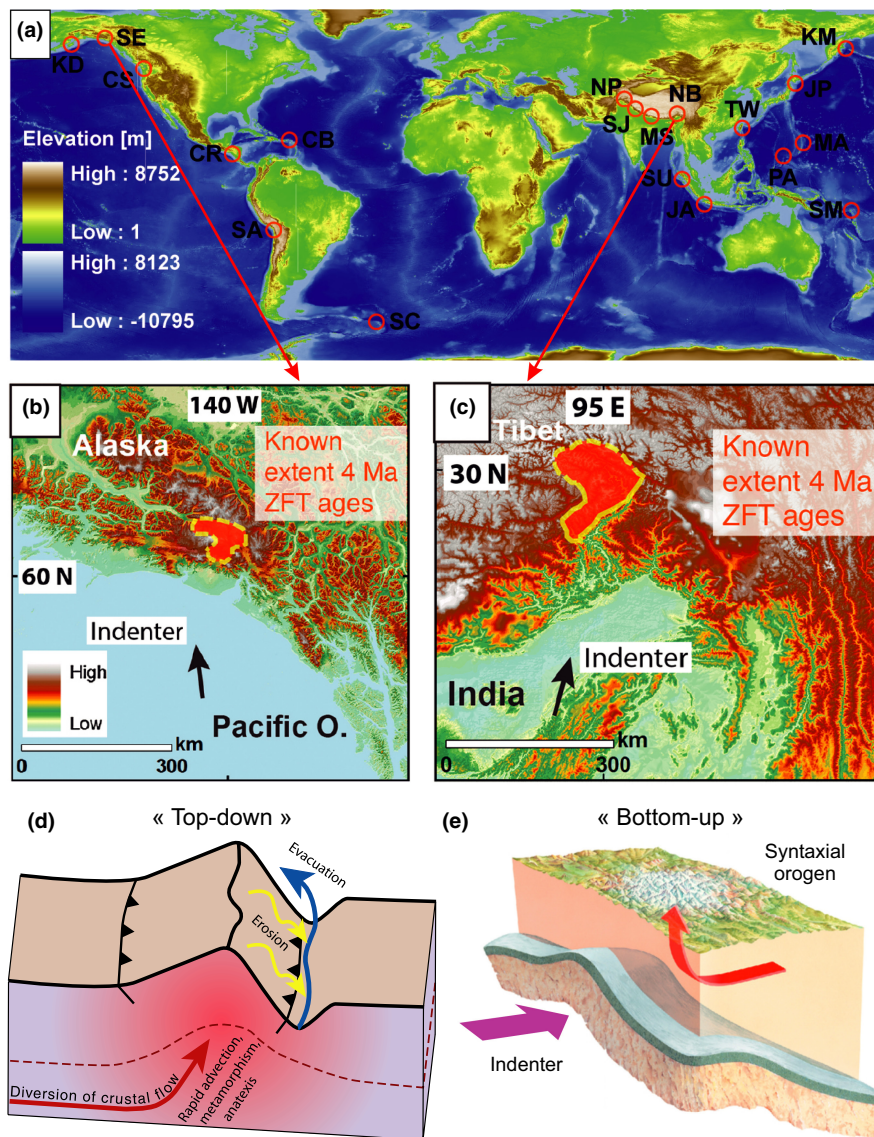


**FIGURE 1** (a) Global plate corner locations (shown by red circles): CB, Caribbean; CR, Costa Rica; CS, Cascadia; SA, South America; SC, South scotia; NP, Nanga Parbat; JA, Java; JP, Japan; KD, Kodiak Island; KM, Kamchatka; MA, Mariana Islands; MS, Marsyandi; NB, Namche Barwa; PA, Palau; SE, St. Elias; SJ, Sutlej; SM, Solomon Islands; SU, Sumatra; TW, Taiwan. (b, c) Known distribution of zircon fission-track (ZFT) ages <4 ma in the mount St. Elias region, Southeast Alaska (Enkelmann et al., 2010; Koons et al., 2013; panel "b") and in the Namche Barwa area, Himalaya (Burg et al., 1998; Enkelmann et al., 2011; panel "c"). The dashed lines represent the inferred extent, with uncertainties due to the limited number of sample sites. Figures are taken from Bendick and Ehlers (2014). (d, e) Schematic representation of two competing models for the origin of localized uplift: "top-down" (panel "d", from Zeitler et al., 2001) and "bottom-up" (panel "e"; from Bendick & Ehlers, 2014) [Colour figure can be viewed at wileyonlinelibrary.com]

design used in our study allow us to investigate the combined impact of geodynamic/tectonic processes and geomorphic/climatic conditions on the development of focused, rapid exhumation.

## 2 | MODEL DESIGN AND MODELLING PROCEDURE

We produced the numerical simulations presented here using the finite element thermo-mechanical code DOUAR (Braun et al., 2008; Thieulot et al., 2008) coupled in 3D with the surface processes code FastScape (Braun & Willett, 2013). For the governing equations and material properties used in the geodynamic and landscape evolution models, and for details on the integration of FastScape into

DOUAR (Figure S1), we refer the reader to the Numerical Methods in Data S1.

A characteristic feature of our model setup (Figure 2) is a 3D bending of the downgoing slab (as required for subduction on a spherical Earth at the plate corners; see Mahadevan et al., 2010) approximated by a central convex-upward-shaped bulge or indenter (Figure 2a,b). The overriding continental plate is modelled as a rheologically stratified lithosphere (Burov, 2011; Burov & Watts, 2006) with an alternation of brittle and ductile layers (Figure 2c).

Since both lithospheric- and mantle-scale numerical studies (e.g., Bonnardot et al., 2008; Schellart et al., 2007) as well as observations from subduction zones (e.g., Ramos & Folguera, 2009) highlight the importance of the internal dynamics of the lower plate for upper plate deformation, the entire downgoing slab (including the indenter bulge)
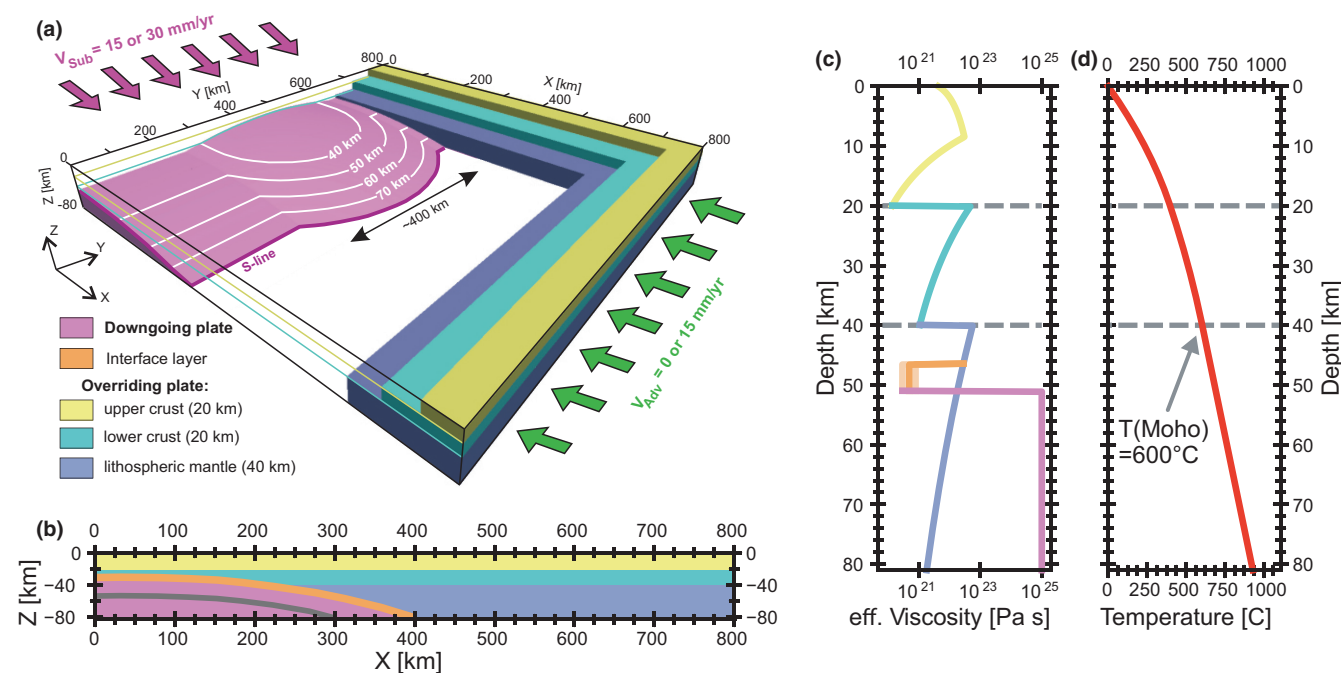


**FIGURE 2** Model setup. (a) 3D view: A vertically layered overriding plate with upper crust, lower crust, and lithospheric mantle, and a subducting plate with a convex-upward-shaped indenter in its central part (between $Y \approx 200$ km and $Y \approx 600$ km; the shape is highlighted by white isolines). The S-line, analogous to the S-point definition of Willett et al. (1993), refers to the intersection of the downgoing plate with the bottom of the model box. Spatial resolution is 6.25 and 1.54 km in horizontal and vertical directions, respectively. At the left ($X = 0$ km) and right ($X = 800$ km) sides of the model domain, uniform and time-independent velocities parallel to $X$-axis are applied. (b) Vertical cross-section along the $X$-axis through the central part of the model domain ($Y = 400$ km). The upper and lower plates are separated by an interface layer whose rheology is of particular interest to this study. The grey line indicates the relative position of the subducting plate along the background (non-indenter) portion outside the central bulge. (c) Vertical profile of the effective viscosity calculated for the initial temperature distribution (see panel "d") and a constant strain rate of $10^{-15}$ s$^{-1}$. Colours denote the different compositional units as in panels "a–b"; lighter shades of the interface layer illustrate the tested viscosity variations. In the overriding lithosphere, the viscous-plastic rheology is temperature-, pressure-, and strain rate-dependent (see Numerical Methods in Data S1): effective viscosity is defined by a Christmas tree-like criterion (Burov, 2011; Ranalli, 1995), assuming ductile flow laws of wet granite and dry diabase (Carter & Tsenn, 1987) for the upper crust and lower crust and the creep law of olivine aggregates (Hirth & Kohlstedt, 2003; Jadamec & Billen, 2012) for the mantle. In contrast, the purely viscous downgoing plate and interface layer are characterized by constant viscosity values of $1 \times 10^{25}$ Pa s and $3$–$8 \times 10^{21}$ Pa s, respectively. (d) Vertical profile of the initial temperature. The nonlinear steady-state geotherm is defined by boundary temperatures of 0°C ($Z = 0$ km) and 930°C ($Z = -80$ km) taking into account radiogenic heat production in the crustal layers. Thermal and rheological parameters are given in Table S1; surface processes parameters can be found in Table S2. To account for the flexural response of the lithosphere to the combined effect of tectonics/geodynamics and erosion/diffusion processes, the upper surface (like all other surfaces in the DOUAR 3D grid) is subjected to an isostatic adjustment calculated for the assumed value of the effective elastic thickness (Burov & Diament, 1995) of 25 km [Colour figure can be viewed at wileyonlinelibrary.com]

is allowed to be deformed (in a ductile manner with constant viscosity; see Figure 2c). To investigate the relative role of the internal deformability of the lower plate, we have also performed several experiments with an absolutely rigid (undeformed) slab which keeps its initial geometry in time as in all previous simulations with similar model setups (Koptev et al., 2019; Nettesheim et al., 2018). In addition, we have also systematically explored the viscosity of the interface layer between the upper and lower plates, which is known to be an important factor in mountain building (e.g., Lamb & Davis, 2003). The ratio between the boundary velocities applied to the right (upper plate advance component) and left (lower plate subduction) sides of the model also represents a variable parameter (see below), while the total shortening rate remains the same in all experiments (30 mm/year).

Overall, we performed numerical simulations for a series of three experiments with four different permutations (12 models in total; Table 1). We do this by varying four controlling parameters including (a) strength of the interface layer (strong, medium or weak); (b) rheology of the lower plate (deformable or rigid); (c) type of surface erosion (total or fluvial); and (d) contribution of upper plate advance in the total shortening (half or none).

The first series (models 1–4) consists of the experiments characterized by total (flat) erosion and half upper plate advance. Here we start with variations in the interface strength from strong to weak for the case of a deformable slab (models 1–3). Subsequently, we test a rigid (undeformable) rheology of the subducting plate in combination with a medium viscosity of the interface layer (model 4). In the second series (models 5–8), we switch the surface erosion from

total to fluvial, while keeping the other parameters as in the first set of models. Finally (the third series; models 9–12), we investigate the velocity boundary conditions without upper plate advance component, keeping the realistically implemented fluvial erosion and varying the interface strength and deformability of the lower plate. Note that in the last set of models, the comparison with a rigid indenter is made for the weak interface layer.

In this study, we analyse not only the resulting distributions of deformation and rock uplift rates but also thermochronometric cooling ages (e.g., Braun, 2003; Ehlers et al., 2005; Huntington et al., 2007; Whipp et al., 2009) which are calculated from the time–temperature history of the tracer particles (Figure S2), thus, providing a proxy for integrated exhumation from the corresponding annealing/retention zone to the surface (Dodson, 1973; Reiners et al., 2005). See Numerical Methods in Data S1 for more detail.

## 3 | RESULTS

### 3.1 | Reference experiment (model 2)

The strain rate distribution of the reference experiment (2_MDTH; Figure 3) is characterized by two oppositely dipping thrust-sense shear zones rooting at the model bottom near its intersection with the subducting plate (see vertical cross-sections in Figure 3d,e). These deep-seated lithospheric-scale faults (Frezzotti et al., 2009; Koptev et al., 2021; Kovács et al., 2020; Vauchez et al., 2012) are accompanied

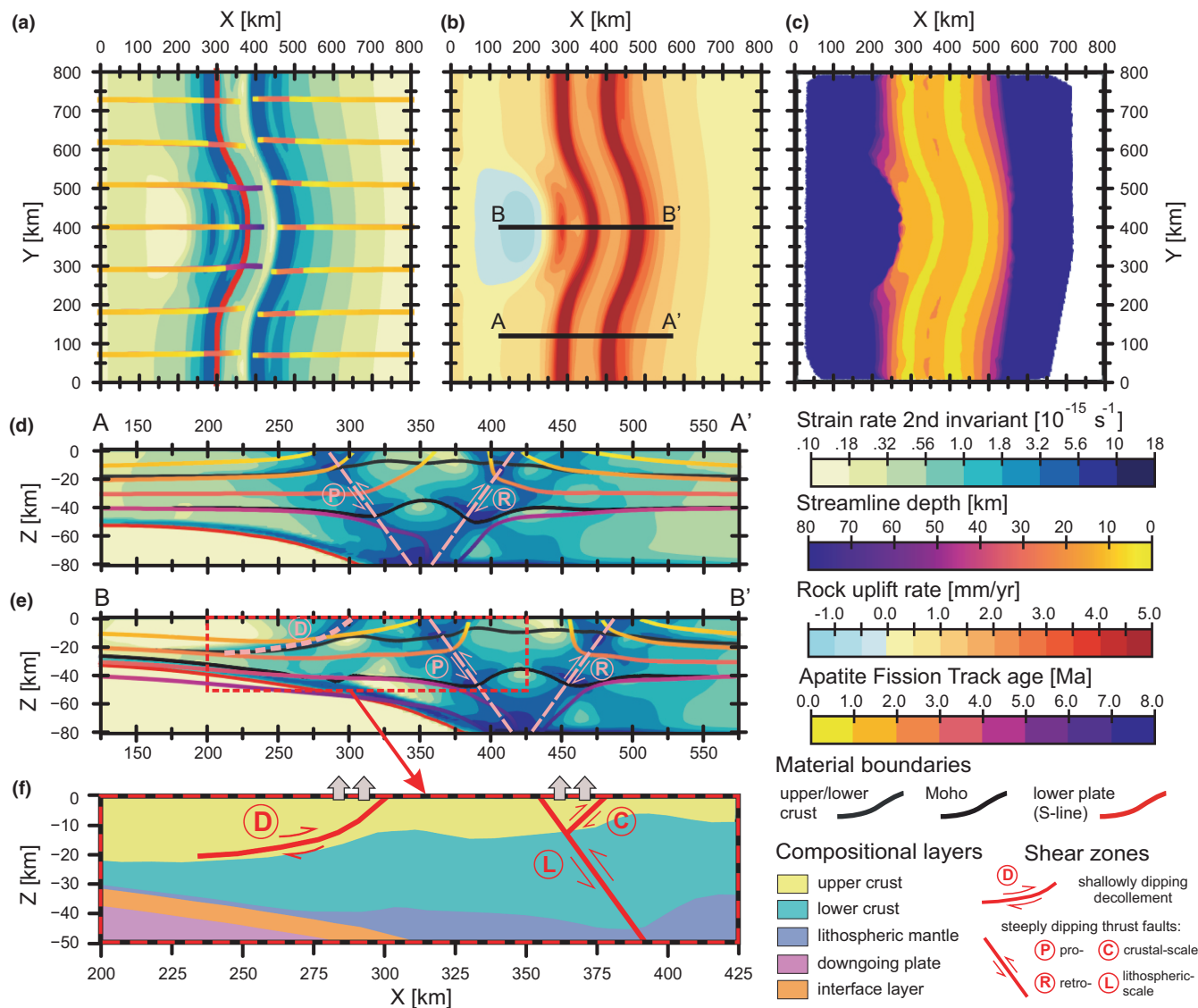**TABLE 1** Controlling parameters of numerical experiments

| Model title | Interface strength | Lower plate deformability | Erosion type | Upper plate advance | Figure | Section |
|---|---|---|---|---|---|---|
| 1_SDTH | Strong | Deformable | Total[b] | Half | 4 | 3.2 |
| 2_MDTH[a] | Medium | Deformable | Total | Half | 3, 4, S2, S3 | 3.1, 3.2 |
| 3_WDTH | Weak | Deformable | Total | Half | 3 | 3.2 |
| 4_MRTH | Medium | Rigid | Total | Half | 3 | 3.2 |
| 5_SDFH | Strong | Deformable | Fluvial[b] | Half | 5 | 3.3 |
| 6_MDFH | Medium | Deformable | Fluvial | Half | 5 | 3.3 |
| 7_WDFH | Weak | Deformable | Fluvial | Half | 5, 7 | 3.3 |
| 8_MRFH | Medium | Rigid | Fluvial | Half | 5 | 3.3 |
| 9_SDFN | Strong | Deformable | Fluvial | None | 6, 7 | 3.4 |
| 10_MDFN | Medium | Deformable | Fluvial | None | 6 | 3.4 |
| 11_WDFN | Weak | Deformable | Fluvial | None | 6, 7, 8 | 3.4 |
| 12_WRFN | Weak | Rigid | Fluvial | None | 6, 7 | 3.4 |

*Note.* The model titles denote the sequence number and identifiers of the four controlling parameters: (1) interface layer strength (viscosity): S (strong, $8 \times 10^{21}$ Pa s), M (medium, $5 \times 10^{21}$ Pa s), or W (weak, $3 \times 10^{21}$ Pa s); (2) lower plate rheology: D (deformable) or R (rigid); (3) surface erosion: T (total) or F (fluvial); and (4) upper plate advance component: H (half) or N (none).

[a]Reference experiment.

[b]In total (or flat) erosion, all of the resulting topography is immediately removed down to the base level. In this case, modelled surface vertical (rock uplift) velocities are equal to the rock exhumation rates (England & Molnar, 1990). More realistic fluvial (and diffusive) erosion is implemented by the FastScape landscape evolution model, which is coupled with the geodynamic code DOUAR in our study (see Numerical Methods in Data S1).

**FIGURE 3** Reference model (2_MDTH: Medium interface strength, deformable lower plate, total erosion, and half upper plate advance) after 6 Myr modelling time. (a–c) Plan views of (a) second invariant of strain rate (at 5 km depth) and particle trajectories (streamlines) originating at 10 and 30 km depth, (b) rock uplift rates, and (c) apatite fission-track (AFT) ages. (d, e) Vertical cross-sections parallel to the *X*-axis show second invariant of strain rate and particle trajectories. (f) Zoom inset shows the kinematics of shallowly dipping decollement and lithospheric- and crustal-scale faults. The black lines in panel "b" show the locations of the vertical cross sections in panels "d–e". Pro- and retro- lithospheric-scale shear zones are labelled by "P" and "R", and shallowly dipping decollement by "D" (panels "d–e"). Crustal- and lithospheric-scale shear zones are labelled by "C" and "L"; grey arrows indicate high exhumation rates (panel "f"). The motion streamlines demonstrate a nearly parallel influx of material from both sides with only a minor component perpendicular to the direction of convergence (panel "a"). The strongest upward motion occurs within small V-shaped wedges squeezed between crustal- and lithospheric-scale shear zones (see particle trajectories originating at 10–20 km depth in panels "d–e"), while the shallowly dipping decollement produces less upward deflection (panel "d"). For details on the temporal evolution of rock uplift at the surface, strain rate in the overriding plate, and internal deformation of the indenter, see Figures S3 and S4 [Colour figure can be viewed at wileyonlinelibrary.com]

by shear zones confined to the upper crust (i.e., crustal-scale shear zones; see Figure 3f). The combination of lithospheric- and crustal-scale faults, that intersect at the vertical level close to the boundary between the upper and lower crust, creates pop-up structures localizing vertical motion between steep fault zones (grey arrows in Figure 3f). As shown in plan view (Figure 3a), both pro- and retro- lithospheric-scale shear zones (as well as associated crustal-scale faults) traverse

the entire model domain in the direction of the Y-axis, forming continuous bands that are elongated perpendicular to subduction and slightly curved towards the overriding plate in the central part above the indenter bulge. The shallow retro-decollement zone rooting into the lower part of the crust forms the third major structure (see central vertical cross-section in Figure 3e). In contrast to steeply dipping pro- and retro-shear zones, this shallowly dipping decollement develops only in

the area above the indenter (Figure 3a) while it attenuates towards the background (non-indenter) portion of the downgoing slab (Figure 3d).

Consistent with the deformation pattern (Figure 3a), the highest rates of rock uplift at the surface (~5–6 mm/year) are concentrated within two narrow bands extending along the pro- and retro-shear zones, while another region of relatively rapid rock uplift (~3–4 mm/year) is located above the indenter (Figure 3b) in the hanging wall of the thrust-sense decollement (Figure 3f). This isolated indenter-centred uplift region, however, remains indiscernible in the field of the predicted apatite fission-track (AFT) ages where it is overshadowed by the two continuous bands of very young ages (<1 Ma) along the trench-parallel S-line (Figure 3c).

## 3.2 | Effect of interface layer strength and subducting plate rheology (models 1–4)

The reduction in the strength of the interface between the upper and downgoing plate leads to higher deformation in the shallow retro-decollement at the expense of the steeply dipping pro- and retro-shear zones which become, in contrast, less pronounced (cf. strain rate distribution of models 1_SDTH, 2_MDTH and 3_WDTH in Figure 4b–d). Accordingly, the localization of rock uplift in the isolated region above the indenter is stronger in the models with a weaker interface layer (Figure 4f–h). The rigid lower plate model (4_MRTH) produces a similar deformation and rock uplift pattern as the experiment with the weak interface (3_WDTH), but with even more active retro-decollement (Figure 4e) resulting in the highest vertical velocities (~5 mm/year) in the hanging wall, which in this case exceeds the localized rock uplift (~3–4 mm/year) in the trench-parallel bands located towards the continent (Figure 4a).

## 3.3 | Effect of erosional efficiency (realistic fluvial erosion; models 5–8)

Switching from total (flat) erosion to more realistic fluvial erosion leads to a general reduction in rock uplift rates, which are distributed over larger areas (cf. Figures 4f–i and 5f–i). Deformation along faults and shear zones is also less localized in the fluvial erosion models (cf. Figures 4b–e and 5b–e). In the experiments with deformable (non-rigid) lower plate, rock uplift rates above the indenter do not exceed ~2.5 mm/year, although it can reach ~3 mm/year and ~4 mm/year at the band related to the retro-shear zone in the models with medium (6_MDFH) and strong (5_SDFH) interface, respectively (Figure 5a). Similar to flat erosion model series, the highest degree of spatial focusing of rock uplift is observed in the rigid slab experiment (8_MRFH; Figure 5i). It is noteworthy that in this model the maximum vertical velocities (~4 mm/year; Figure 5a) localized within the indenter-centred region are associated with a small pop-up structure (crustal-scale wedge confined between oppositely dipping shear zones; Figure 5e) rather than a shallowly dipping decollement as in the case of the flat-erosion counterpart (Figure 4e).

## 3.4 | Effect of velocity boundary conditions (no upper plate advance; models 9–12)

In the models with lateral shortening provided only by subduction (i.e., without an upper plate advance component), most of the deformation is localized in the pro-shear zone that nucleates where the subducting plate intersects the overriding plate's Moho (models with strong (9_SDFN) and medium (10_MDFN) interface; Figure 6b,c) or in a crustal-scale indenter-centred wedge (models with weak interface (11_WDFN) and undeformable indenter (12_WRFN); Figure 6d,e). The area of focused uplift associated with these structures (Figure 6f–i) migrates towards the downgoing plate as the strength of the interface layer decreases (Figure 6a). The experiment with a weak interface and deformable lower plate (11_WDFN) produces the highest maximum rock uplift rates (~6 mm/year; Figure 6a) which are confined to an isolated region above the indenter (Figure 6h). This result is in contrast to the models with stronger interface (9_SDFN and 10_MDFN; Figure 6f,g) where localized uplift also occurs along the entire length of the background slab segment (i.e., non-indenter portion outside the central bulge; see Figure 2). The rigid lower plate model (12_WRFN) shows focused indenter-centred uplift (Figure 6i) but at a lower maximum rate (~4.5 mm/year; Figure 6a). The localization of the strain rate in the crustal pop-up structure is also less pronounced compared to the corresponding experiment with deformable subducting slab (cf. Figure 6d,e).

## 4 | DISCUSSION

Large thrust fault systems dipping in opposite (pro- and retro-)directions (e.g., Contact Fault and Border Ranges Fault in the Yakutat collision zone of southeast Alaska; Arkle et al., 2013) are characteristic features of many continental orogens described as "doubly vergent" (Argand, 1916; Eizenhöfer et al., 2021; Willett et al., 1993). Our results show that a higher viscosity of the interface layer (i.e., a stronger mechanical connection between the subducting and overriding plate) favours deformation accommodation along trench-parallel lithospheric-scale shear bands and, therefore, reduces the influence of the curved geometry of the subducting plate (i.e., the central indenter bulge) on the overall rock uplift patterns. A weaker interface, in contrast, enhances the indenter-centred fault structures (shallowly dipping retro-decollement or crustal-scale wedge) and focuses the rock uplift in the isolated region above. Note that although many decollement layers have been observed in the thrust belts around the world (Sommaruga, 1999; Tang et al., 2008) and their role has been extensively studied in both analogue (Koyi & Vendeville, 2003; Pichot & Nalpas, 2009) and numerical (Feng et al., 2015; Ruh et al., 2012) approaches, a decollement dipping in the foreland (or retro) direction is less likely to correspond to known geological settings in nature. Importantly, such retro-dipping decollement is reproduced only in experiments that assume an unrealistically high erosional efficiency (Figures 3 and 4). In contrast, in models with realistically implemented fluvial erosion,
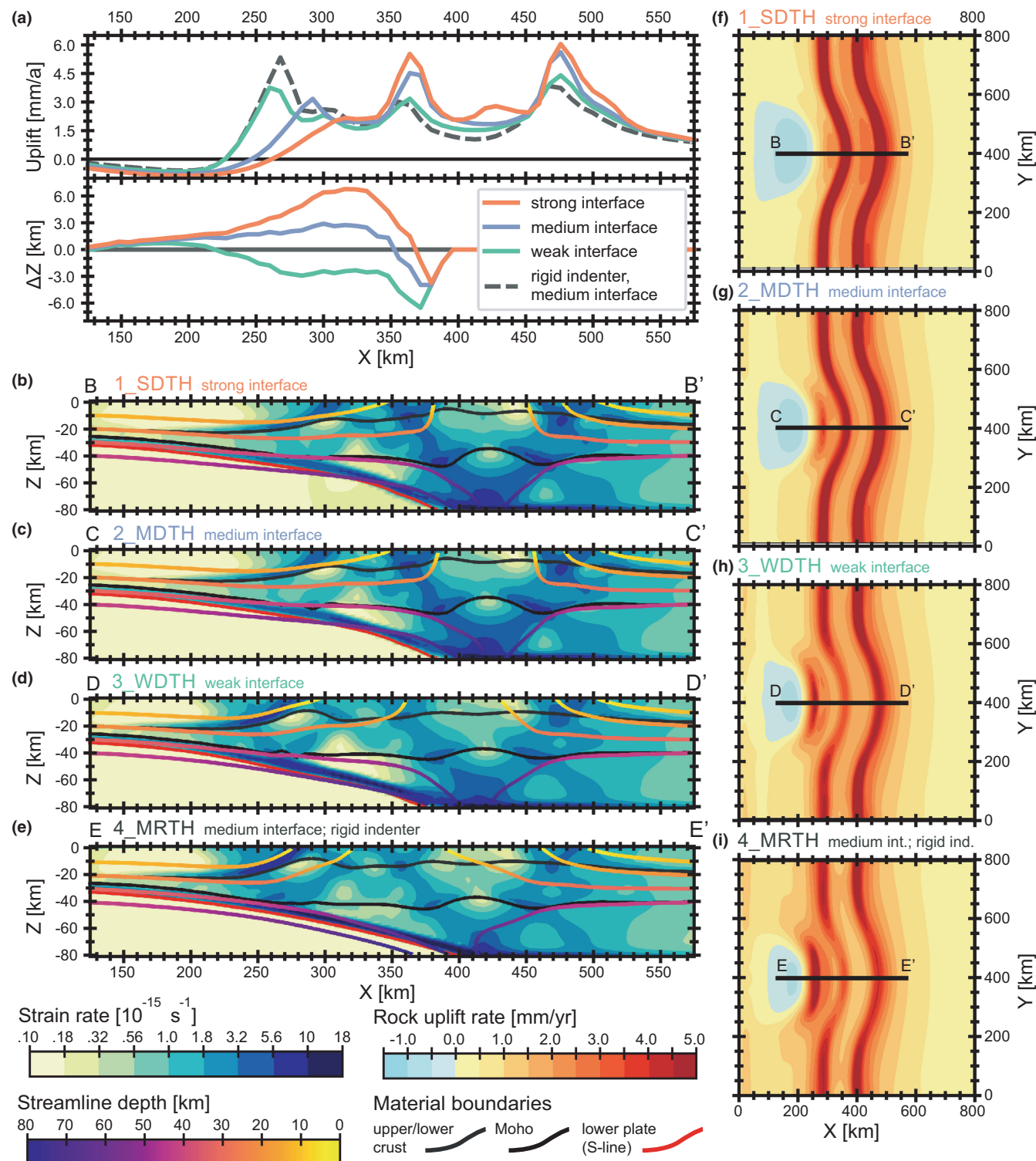
**FIGURE 4** Models with variable strength of the interface layer and deformability of the lower plate (1_SDTH, 2_MDTH, 3_WDTH, and 4_MRTH) after 6 Myr modelling time. (a) Rock uplift rates and indenter deformation along the profile at $Y = 400$ km. (b–e) Vertical cross-sections parallel to the $X$-axis show second invariant of strain rate and motion streamlines. (f–i) Plan views of rock uplift rates. The location of the profiles and cross-sections in panels "a–e" is shown by the black lines in panels "f–i". Note that the upward deformation of the indenter is strongest in the strong interface model (1_SDTH; panel "a", lower part), but this is not reflected in the rock uplift at the surface, which is better expressed in the experiments with weaker interface (panel "a", upper part) [Colour figure can be viewed at wileyonlinelibrary.com]

indenter-centred uplift is usually associated with a small pop-up structure squeezed between the crustal-scale pro- and retro-shear zones (Figures 5 and 6).

The deformability of the lower plate has a twofold effect: under the boundary conditions of half upper plate advance, a rigid slab intensifies localized uplift above the indenter, while the opposite
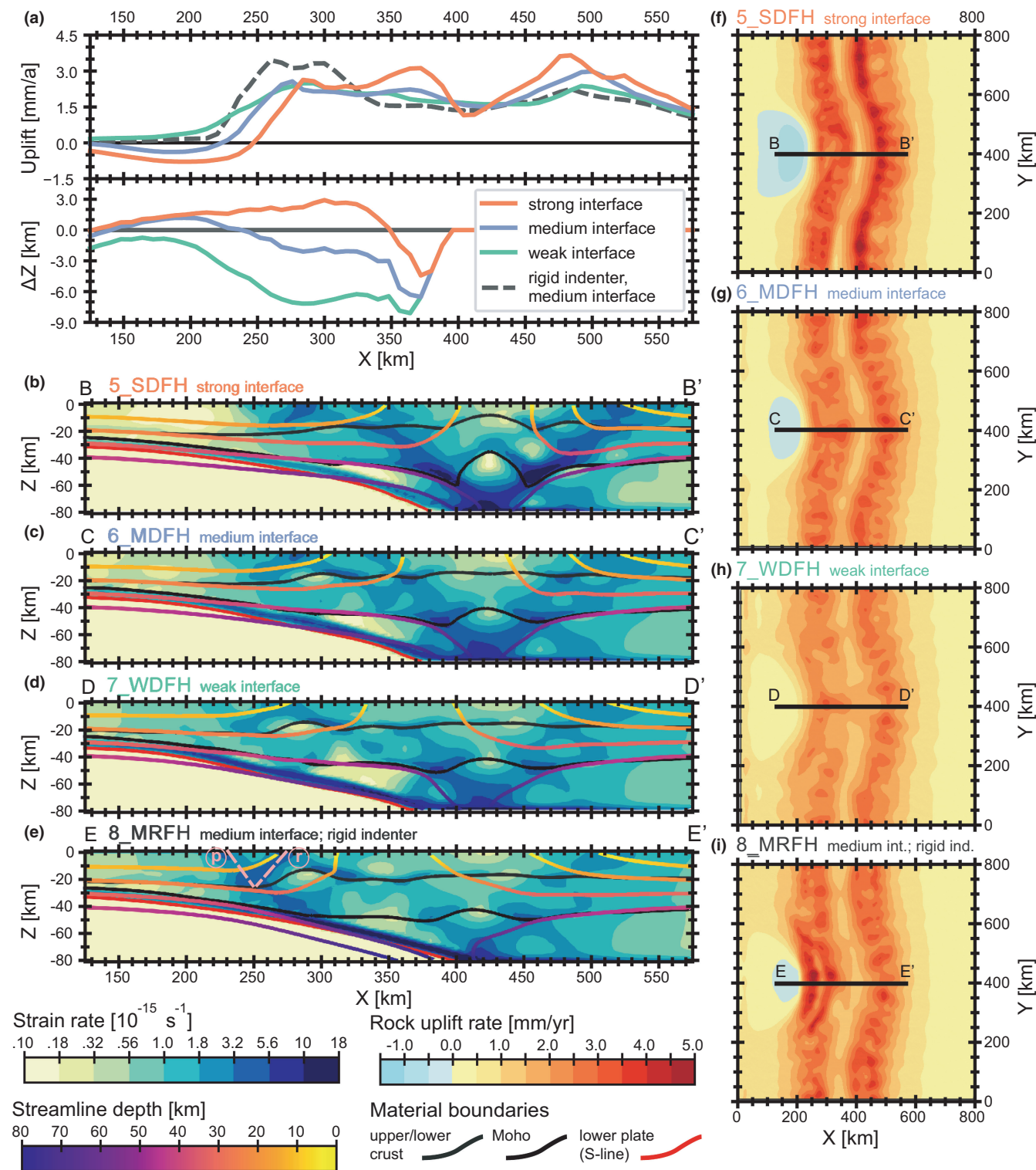
**FIGURE 5** Models with realistically implemented fluvial (non-flat) erosion (5_SDFH, 6_MDFH, 7_WDFH, and 8_MRFH) after 6 Myr modelling time. Figure conventions as in Figure 4. Note that in the models with strong (5_SDFH) and medium (6_MDFH) interface, shortening is predominantly accommodated by the two large (lithospheric-scale) shear zones rooting at the S-line (panels "b" and "c") whereas the reduction of the interface layer strength (model 7_WDFH) and the switching to an undeformable (rigid) lower plate (model 8_MRFH) result in strain localization within smaller shear zones rooting at the Moho directly above the indenter apex (panels "d" and "e"). In panel "e", the corresponding crustal-scale pro- and retro-shear zones are labelled by "p" and "r". Oppositely dipping thrust faults have been commonly reproduced in previous 2D (Vogt et al., 2017; Auzemery et al., 2021) and 3D (Braun & Yamato, 2010; Ruh et al., 2013) numerical studies investigating the accumulation and localization of deformation in convergent geodynamic environments [Colour figure can be viewed at wileyonlinelibrary.com]
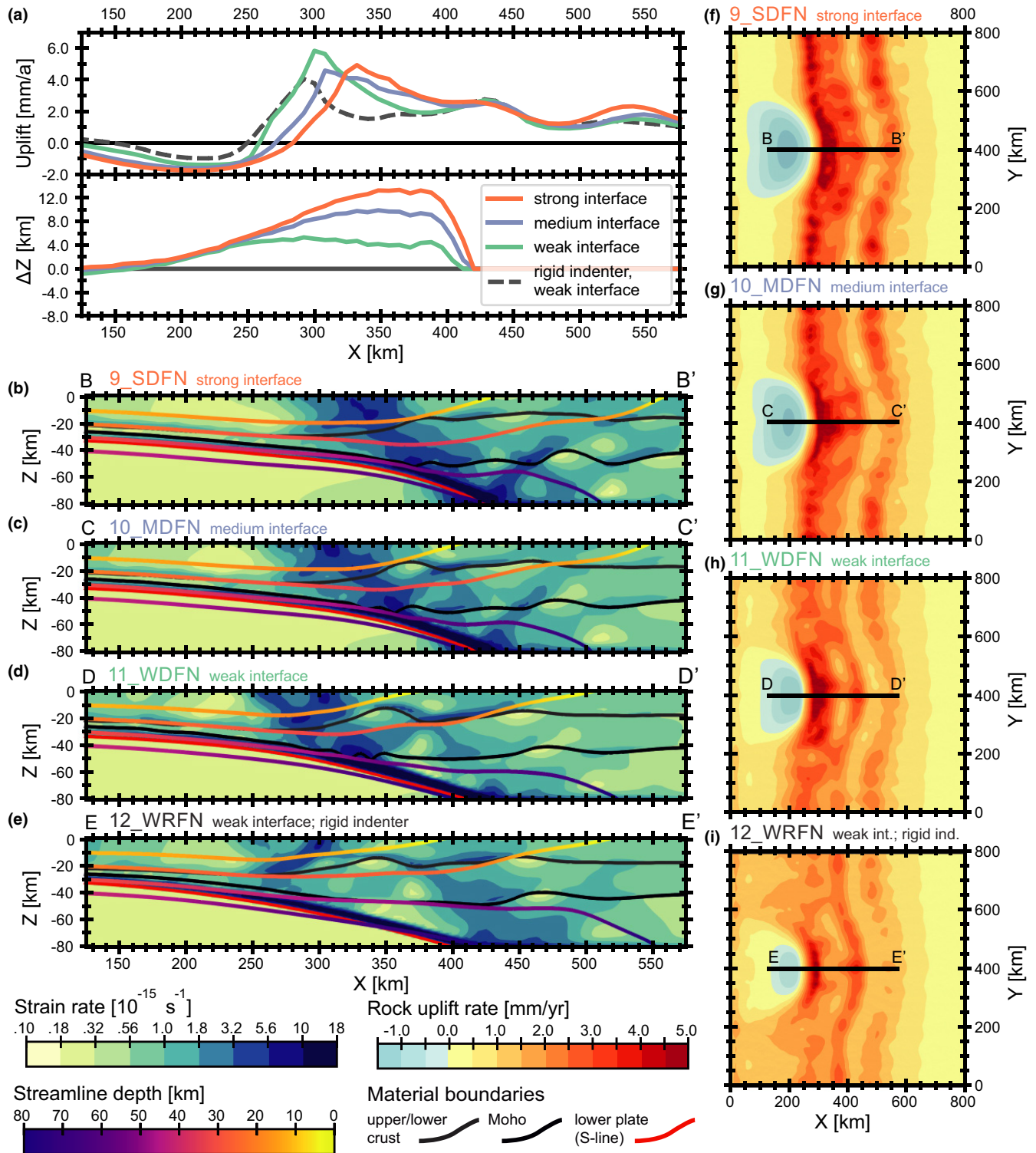
**FIGURE 6** Models with realistically implemented fluvial (non-flat) erosion and under no upper plate advance (9_SDFN, 10_MDFN, 11_WDFN, and 12_WRFN) after 6 Myr modelling time. Figure conventions as in Figure 4. Note that unlike the previous model series (Figures 4 and 5), the experiment with rigid lower plate (12_WRFN) does not have the highest uplift rate, which is lower than in the experiment with deformable slab and weak interface layer (11_WDFN; see panel "a") [Colour figure can be viewed at wileyonlinelibrary.com]

is found for the models without upper plate advance component. Another important aspect of the no upper plate advance case is a much more focused, and faster, rock uplift compared to the corresponding half-advance scenarios.

The highest rock uplift rates (up to ~6 mm/year), focused within an isolated indenter-centred region, are found in model 11_WDFN (Figure 7a), which is characterized by a weak interface layer, a deformable lower plate, realistic fluvial erosion and no upper plate
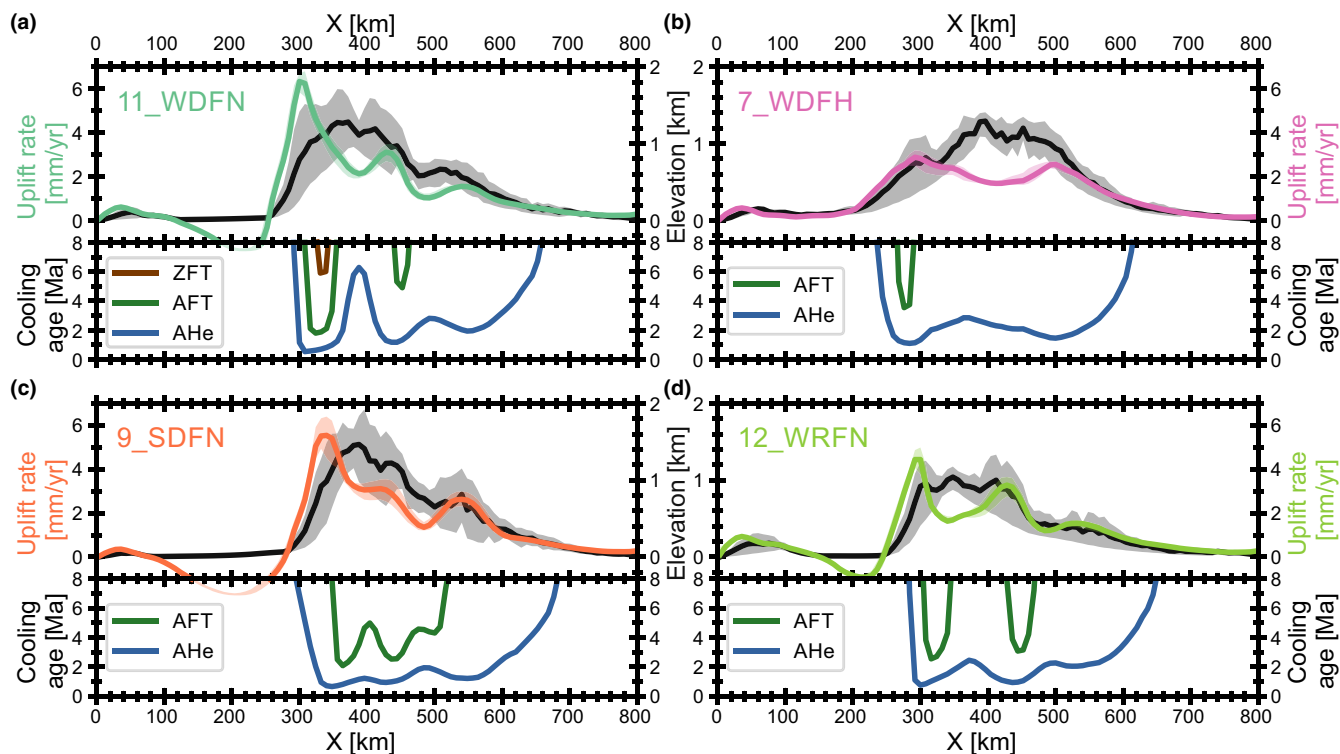
**FIGURE 7** Swath profiles of rock uplift rates, topography (upper panels), and apatite (U-Th)/he (AHe), apatite fission-track (AFT), and zircon fission-track (ZFT) ages (lower panels) for the following fluvial erosion scenarios after 6 Myr modelling time: (a) 11_WDFN (weak interface, deformable slab, and no upper plate advance); (b) 7_WDFH (same as 11_WDFN but half upper plate advance); (c) 9_SDFN (same as 11_WDFN but strong interface); and (d) 12_WRFN (same as 11_WDFN but rigid slab). All profiles are located in the central part of the model (Y = 400 km) and oriented parallel to the convergence direction. It should be noted that the highest uplift rates occur along orogen slopes, preferentially in steep valleys with high erosion potential (see Nettesheim et al., 2018 for more details). The minima in the predicted cooling ages are also slightly shifted with respect to the highest local relief. AFT ages are more representative of these settings because the modelled uplift rates are too high to generate much variance in the predicted AHe ages. ZFT ages are shown only for the model 11_WDFN, as they are completely unreset in the other cases [Colour figure can be viewed at wileyonlinelibrary.com]

advance. Switching to half upper plate advance (model 7_WDFH) results in a nearly symmetric profile of rock uplift rates and reduces their maximum value significantly (to ~2.5 mm/year; Figure 7b). Increasing the interface strength (model 9_SDFN) allows maximum vertical velocities to remain sufficiently high (~5 mm/year), but de-localizes rock exhumation spatially, forming a broad (~200 km) area of relatively rapid rock uplift (>3 mm/year), which is also reflected in young (<4 Ma) AFT ages (Figure 7c). In contrast, the transition to a rigid indenter (model 12_WRFN) avoids spatial defocusing of exhumation while reducing the amplitude of maximum uplift rates to ~4.5 mm/year (Figure 7d).

It is noteworthy that even a simplified setting with flat erosion and a rigid downgoing slab (model 4_MRTH) is able to generate high and isolated rock uplift above the indenter (Figure 4a,i). However, as shown in previous work by Koptev et al. (2019), such extremely high erosional efficiency always promotes a significant overestimation of total rock exhumation, resulting in unrealistically young AFT ages (<1 Ma) systematically predicted within bull's eye structures. Implementation of realistic fluvial erosion at the surface is therefore an essential requirement for successful reproduction of not only the general exhumation patterns but also the thermochronometric ages observed in the plate corners. The temporal acceleration of rock
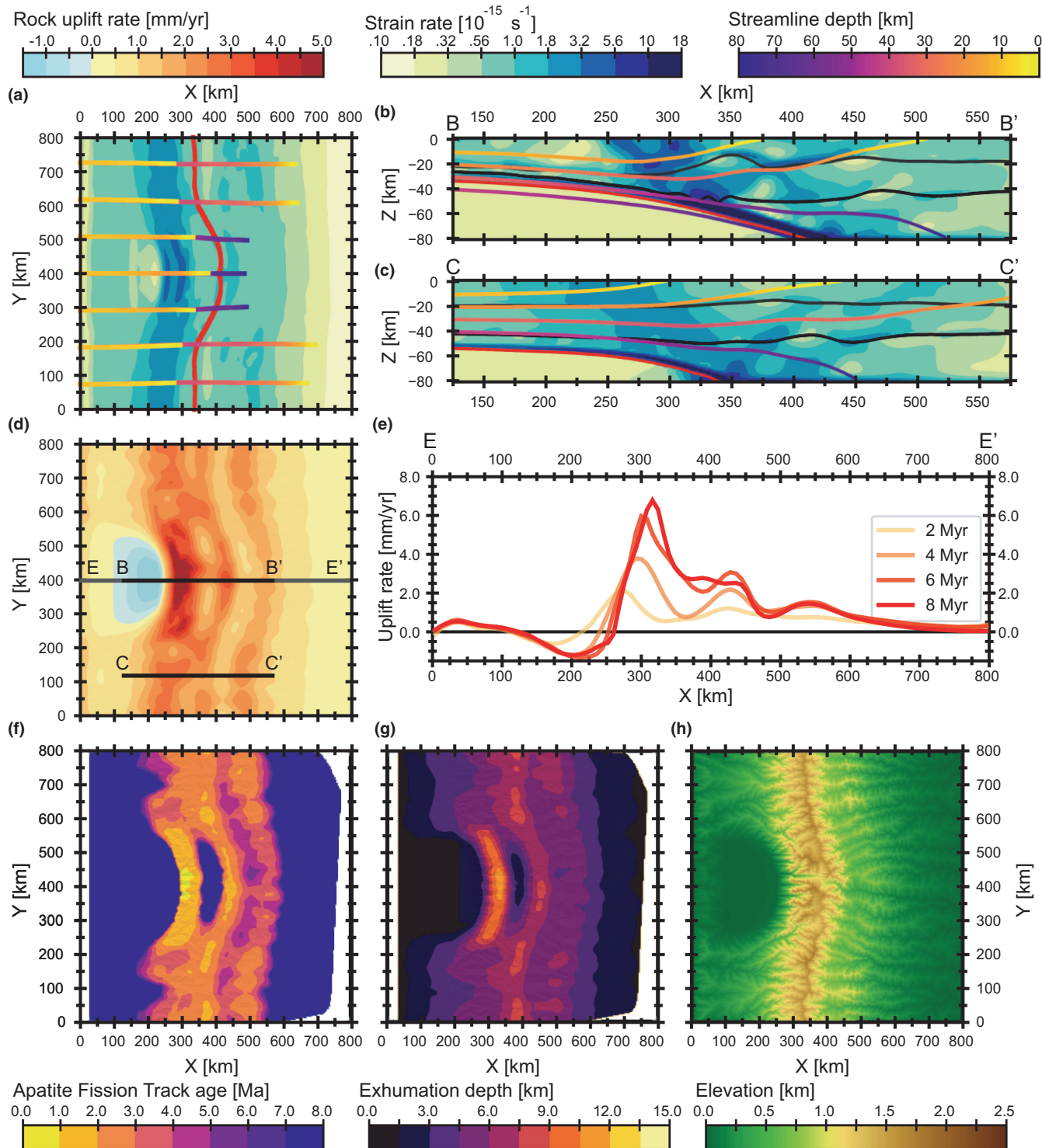
uplift and exhumation (see Figure 8) is also indicative of the close link between tectonic forcing and focused surface erosion (e.g., Sharma et al., 2021).

## 5 | CONCLUSIONS

The results presented here reveal that first-order characteristics of the thermochronometer age patterns observed in "syntaxial orogens" can be reproduced in numerical experiments under the condition of a deformable subduction slab and a rheologically stratified overriding plate on one hand, and a realistic implementation of the landscape evolution model on the other hand. This suggests that the extreme localized exhumation often detected at the corners of convergent plate boundaries is caused by combined and mutually reinforcing influences of factors such as rheologically controlled tectonic deformation in the crust and lithospheric mantle, and fluvial erosion processes at the surface.

Although it has been known for more than two decades that surface erosion and associated sediment transport and deposition exert a first-order control on crustal stresses and fault activity (Burov & Cloetingh, 1997; Burov & Poliakov, 2001, 2003; Van Balen

**FIGURE 8** Overall view of the model 11_WDFN (weak interface, deformable slab, fluvial erosion, and no upper plate advance) after 6 Myr modelling time. (a) Plan view of second invariant of strain rate (at 5 km depth) and particle trajectories (streamlines) originating at 10 km and 30 km depth. (b, c) Vertical cross-sections parallel to the X-axis show second invariant of strain rate and particle trajectories. (d) Plan view of rock uplift rates. (e) Temporal evolution of rock uplift rates along the profile at Y = 400 km. (f–h) Plan views of (f) apatite fission-track (AFT) ages, (g) exhumation depth, and (h) topography elevation. The locations of the profile and cross-sections in panels "b", "c", and "e" are shown by the grey and black lines in panel "d". Note that in the early stages of model development, rock uplift rates are 1.8 times faster on the left summit than on the right summit (2.3 mm/year vs. 1.3 mm/year for X = 280 km and X = 420 km, respectively, after 2 Myr modelling time), while this ratio increases to 2.7 after 8 Myr modelling time (6.8 mm/year vs. 2.5 mm/year; see panel "e") [Colour figure can be viewed at wileyonlinelibrary.com]

et al., 1995), most hybrid geomorphological-geodynamic modelling studies are still limited to 2D analysis (e.g., Ballato et al., 2019; Beucher & Huismans, 2020; Burov et al., 2014; Neuharth et al., 2022; Sternai, 2020) and/or to a simplified, diffusion-only implementation of the surface processes (e.g., Neuharth et al., 2021; Ruh et al., 2013). However, many tectonic and geodynamic structures and processes are inherently 3D nature (Gerya, 2019), and regional denudation rates and patterns in tectonically active areas with relatively steep topography are primarily controlled not by diffusion but rather by the efficiency of processes influencing river erosion (Schmid et al., 2018; Starke et al., 2020; Whipple, 2004). In this context, recently developed numerical techniques that couple thermo-mechanical geodynamic models with simulations of realistic (including fluvial erosion) landscape evolution in 3D (Braun & Yamato, 2010; Collignon et al., 2014; Thieulot et al., 2014; Ueda et al., 2015; Nettesheim et al., 2018; this study) should be used more widely in future research.

## ACKNOWLEDGEMENTS

## CONFLICT OF INTEREST

The authors declare that there is no conflict of interest.

## DATA AVAILABILITY STATEMENT

The data that supports the findings of this study are available within the article and Supporting Information.

## REFERENCES

Adams, B. A., & Ehlers, T. A. (2017). Deciphering topographic signals of glaciation and rock uplift in an active orogen: A case study from the Olympic Mountains, USA. *Earth Surface Processes and Landforms*, *42*(11), 1680–1692.

Argand, E. (1916). Sur l'arc des Alpes occidentales. *Ecologae Geologicae Helvetiae*, *14*, 145–191.

Arkle, J. C., Armstrong, P. A., Haeussler, P. J., Prior, M. G., Hartman, S., Sendziak, K. L., & Brush, J. A. (2013). Focused exhumation in the syntaxis of the western Chugach Mountains and Prince William sound, Alaska. *GSA Bulletin*, *125*(5–6), 776–793.

Artyushkov, E. V., Kol'ka, V. V., & Chekhovich, P. A. (2020). The occurrence of a lower viscosity layer in the crust of old cratons as a cause of the strongly differentiated character of postglacial uplift. *Doklady Earth Sciences*, *492*(1), 351–355.

Artyushkov, E. V., Korikovsky, S. P., Massonne, H. J., & Chekhovich, P. A. (2018). Recent crustal uplift of Precambrian cratons: Key patterns and possible mechanisms. *Russian Geology and Geophysics*, *59*(11), 1389–1409.

Auzemery, A., Yamato, P., Duretz, T., Willingshofer, E., Matenco, L., & Porkoláb, K. (2021). Influence of magma-poor versus magma-rich passive margins on subduction initiation. *Gondwana Research*, *103*, 172–186.

Ballato, P., Brune, S., & Strecker, M. R. (2019). Sedimentary loading-unloading cycles and faulting in intermontane basins: Insights from numerical modeling and field observations in the NW argentine Andes. *Earth and Planetary Science Letters*, *506*, 388–396.

Bendick, R., & Ehlers, T. A. (2014). Extreme localized exhumation at syntaxes initiated by subduction geometry. *Geophysical Research Letters*, *41*(16), 5861–5867.

Berger, A. L., Spotila, J. A., Chapman, J. B., Pavlis, T. L., Enkelmann, E., Ruppert, N. A., & Buscher, J. T. (2008). Architecture, kinematics, and exhumation of a convergent orogenic wedge: A thermochronological investigation of tectonic-climatic interactions within the central St. Elias orogen, Alaska. *Earth and Planetary Science Letters*, *270*(1–2), 13–24.

Beucher, R., & Huismans, R. S. (2020). Morphotectonic evolution of passive margins undergoing active surface processes: Large-scale experiments using numerical models. *Geochemistry, Geophysics, Geosystems*, *21*(5), e2019GC008884.

Bonnardot, M. A., Hassani, R., Tric, E., Ruellan, E., & Régnier, M. (2008). Effect of margin curvature on plate deformation in a 3-D numerical model of subduction zones. *Geophysical Journal International*, *173*(3), 1084–1094.

Brandon, M. T., Roden-Tice, M. K., & Garver, J. I. (1998). Late Cenozoic exhumation of the Cascadia accretionary wedge in the Olympic Mountains, Northwest Washington state. *GSA Bulletin*, *110*(8), 985–1009.

Braun, J. (2003). Pecube: A new finite-element code to solve the 3D heat transport equation including the effects of a time-varying, finite amplitude surface topography. *Computers & Geosciences*, *29*(6), 787–794.

Braun, J., Thieulot, C., Fullsack, P., DeKool, M., Beaumont, C., & Huismans, R. (2008). DOUAR: A new three-dimensional creeping flow numerical model for the solution of geological problems. *Physics of the Earth and Planetary Interiors*, *171*(1–4), 76–91.

Braun, J., & Willett, S. D. (2013). A very efficient O (n), implicit and parallel method to solve the stream power equation governing fluvial incision and landscape evolution. *Geomorphology*, *180*, 170–179.

Braun, J., & Yamato, P. (2010). Structural evolution of a three-dimensional, finite-width crustal wedge. *Tectonophysics*, *484*(1–4), 181–192.

Burg, J. P., Nievergelt, P., Oberli, F., Seward, D., Davy, P., Maurin, J. C., Diao, Z., & Meier, M. (1998). The Namche Barwa syntaxis: Evidence for exhumation related to compressional crustal folding. *Journal of Asian Earth Sciences*, *16*(2–3), 239–252.

Burov, E., & Cloetingh, S. A. P. L. (1997). Erosion and rift dynamics: New thermomechanical aspects of post-rift evolution of extensional basins. *Earth and Planetary Science Letters*, *150*(1–2), 7–26.

Burov, E., François, T., Agard, P., Le Pourhiet, L., Meyer, B., Tirel, C., Lebedev, S., Yamato, P., & Brun, J. P. (2014). Rheological and geodynamic controls on the mechanisms of subduction and HP/UHP exhumation of crustal rocks during continental collision: Insights from numerical models. *Tectonophysics*, *631*, 212–250.

Burov, E., & Poliakov, A. (2001). Erosion and rheology controls on syn-rift and postrift evolution: Verifying old and new ideas using a fully coupled numerical model. *Journal of Geophysical Research: Solid Earth*, *106*(B8), 16461–16481.

Burov, E., & Poliakov, A. (2003). Erosional forcing of basin dynamics: New aspects of syn-and post-rift evolution. *Geological Society, London, Special Publications*, *212*(1), 209–223.

Burov, E. B. (2011). Rheology and strength of the lithosphere. *Marine and Petroleum Geology*, *28*(8), 1402–1443.

Burov, E. B., & Diament, M. (1995). The effective elastic thickness (T e) of continental lithosphere: What does it really mean? *Journal of Geophysical Research: Solid Earth*, 100(B3), 3905–3927.

Burov, E. B., & Watts, A. B. (2006). The long-term strength of continental lithosphere: "Jelly sandwich" or" crème brûlée"? *GSA Today*, 16(1), 4–10.

Carter, N. L., & Tsenn, M. C. (1987). Flow properties of continental lithosphere. *Tectonophysics*, 136(1–2), 27–63.

Collignon, M., Kaus, B. J. P., May, D. A., & Fernandez, N. (2014). Influences of surface processes on fold growth during 3-D detachment folding. *Geochemistry, Geophysics, Geosystems*, 15(8), 3281–3303.

Crowley, J. L., Waters, D. J., Searle, M. P., & Bowring, S. A. (2009). Pleistocene melting and rapid exhumation of the Nanga Parbat massif, Pakistan: Age and P-T conditions of accessory mineral growth in migmatite and leucogranite. *Earth and Planetary Science Letters*, 288(3–4), 408–420.

Dodson, M. H. (1973). Closure temperature in cooling geochronological and petrological systems. *Contributions to Mineralogy and Petrology*, 40(3), 259–274.

Ehlers, T. A., Chaudhri, T., Kumar, S., Fuller, C. W., Willett, S. D., Ketcham, R. A., Brandon, M. T., Belton, D. X., Kohn, B. R., Gleadow, A. J. W., Dunai, T. J., & Fu, F. Q. (2005). Computational tools for low-temperature thermochronometer interpretation. *Reviews in Mineralogy and Geochemistry*, 58(1), 589–622.

Eizenhöfer, P. R., Glotzbach, C., Büttner, L., Kley, J., & Ehlers, T. A. (2021). Turning the orogenic switch: Slab-reversal in the eastern Alps recorded by low-temperature thermochronology. *Geophysical Research Letters*, 48(6), e2020GL092121.

England, P., & Molnar, P. (1990). Surface uplift, uplift of rocks, and exhumation of rocks. *Geology*, 18(12), 1173–1177.

Enkelmann, E., Ehlers, T. A., Zeitler, P. K., & Hallet, B. (2011). Denudation of the Namche Barwa antiform, eastern Himalaya. *Earth and Planetary Science Letters*, 307(3–4), 323–333.

Enkelmann, E., Piestrzeniewicz, A., Falkowski, S., Stübner, K., & Ehlers, T. A. (2017). Thermochronology in Southeast Alaska and Southwest Yukon: Implications for north American plate response to terrane accretion. *Earth and Planetary Science Letters*, 457, 348–358.

Enkelmann, E., Zeitler, P. K., Garver, J. I., Pavlis, T. L., & Hooks, B. P. (2010). The thermochronological record of tectonic and surface process interaction at the Yakutat-north American collision zone in Southeast Alaska. *American Journal of Science*, 310(4), 231–260.

Falkowski, S., Enkelmann, E., Drost, K., Pfänder, J. A., Stübner, K., & Ehlers, T. A. (2016). Cooling history of the St. Elias syntaxis, Southeast Alaska, revealed by geochronology and thermochronology of cobble-sized glacial detritus. *Tectonics*, 35(2), 447–468.

Falkowski, S., Enkelmann, E., & Ehlers, T. A. (2014). Constraining the area of rapid and deep-seated exhumation at the St. Elias syntaxis, Southeast Alaska, with detrital zircon fission-track analysis. *Tectonics*, 33(5), 597–616.

Feng, L., Bartholomew, M. J., & Choi, E. (2015). Spatial arrangement of décollements as a control on the development of thrust faults. *Journal of Structural Geology*, 75, 49–59.

Frezzotti, M. L., Peccerillo, A., & Panza, G. (2009). Carbonate metasomatism and CO2 lithosphere-asthenosphere degassing beneath the Western Mediterranean: An integrated model arising from petrological and geophysical data. *Chemical Geology*, 262(1–2), 108–120.

Gerya, T. (2019). *Introduction to numerical geodynamic modelling* (2nd ed., p. 471). Cambridge University Press.

Hirth, G., & Kohlstedt, D. (2003). Rheology of the upper mantle and the mantle wedge: A view from the experimentalists. *Geophysical Monograph - American Geophysical Union*, 138, 83–106.

Huntington, K. W., Ehlers, T. A., Hodges, K. V., & Whipp, D. M., Jr. (2007). Topography, exhumation pathway, age uncertainties, and the interpretation of thermochronometer data. *Tectonics*, 26(4), TC4012.

Jadamec, M. A., & Billen, M. I. (2012). The role of rheology and slab shape on rapid mantle flow: Three-dimensional numerical models of the Alaska slab edge. *Journal of Geophysical Research: Solid Earth*, 117(B2), B02304.

Koons, P. O., Hooks, B. P., Pavlis, T., Upton, P., & Barker, A. D. (2010). Three-dimensional mechanics of Yakutat convergence in the southern Alaskan plate corner. *Tectonics*, 29(4), TC4008.

Koons, P. O., Zeitler, P. K., Chamberlain, C. P., Craw, D., & Meltzer, A. S. (2002). Mechanical links between erosion and metamorphism in Nanga Parbat, Pakistan Himalaya. *American Journal of Science*, 302(9), 749–773.

Koons, P. O., Zeitler, P. K., & Hallet, B. (2013). Tectonic aneurysms and mountain building. In *Treatise on geomorphology* (Vol. 5, pp. 318–349). Elsevier.

Koptev, A., Cloetingh, S., Kovács, I. J., Gerya, T., & Ehlers, T. A. (2021). Controls by rheological structure of the lithosphere on the temporal evolution of continental magmatism: Inferences from the Pannonian Basin system. *Earth and Planetary Science Letters*, 565, 116925.

Koptev, A., Ehlers, T. A., Nettesheim, M., & Whipp, D. M. (2019). Response of a rheologically stratified lithosphere to subduction of an indenter-shaped plate: Insights into localized exhumation at orogen syntaxes. *Tectonics*, 38(6), 1908–1930.

Kovács, I., Patkó, L., Liptai, N., Lange, T. P., Taracsák, Z., Cloetingh, S. A. P. L., Török, K., Király, E., Karátson, D., Biró, T., Kiss, J., Pálos, Z., Aradi, L. E., Falus, G., Hidas, K., Berkesi, M., Koptev, A., Novák, A., Wesztergom, V., … Szabó, C. (2020). The role of water and compression in the genesis of alkaline basalts: Inferences from the Carpathian-Pannonian region. *Lithos*, 354, 105323.

Koyi, H. A., & Vendeville, B. C. (2003). The effect of décollement dip on geometry and kinematics of model accretionary wedges. *Journal of Structural Geology*, 25(9), 1445–1450.

Lamb, S., & Davis, P. (2003). Cenozoic climate change as a possible cause for the rise of the Andes. *Nature*, 425(6960), 792–797.

Lang, K. A., Huntington, K. W., Burmester, R., & Housen, B. (2016). Rapid exhumation of the eastern Himalayan syntaxis since the late Miocene. *GSA Bulletin*, 128(9–10), 1403–1422.

Mahadevan, L., Bendick, R., & Liang, H. (2010). Why subduction zones are curved. *Tectonics*, 29(6), TC6002.

Michel, L., Ehlers, T. A., Glotzbach, C., Adams, B. A., & Stübner, K. (2018). Tectonic and glacial contributions to focused exhumation in the Olympic Mountains, Washington, USA. *Geology*, 46(6), 491–494.

Nettesheim, M., Ehlers, T. A., Whipp, D. M., & Koptev, A. (2018). The influence of upper-plate advance and erosion on overriding plate deformation in orogen syntaxes. *Solid Earth*, 9(6), 1207–1224.

Neuharth, D., Brune, S., Glerum, A., Morley, C. K., Yuan, X., & Braun, J. (2021). Flexural strike-slip basins. *Geology*. https://doi.org/10.1130/G49351.1

Neuharth, D., Brune, S., Wrona, T., Glerum, A., Braun, J., & Yuan, X. (2022). Evolution of rift systems and their fault networks in response to surface processes. *Tectonics*, e2021TC007166.

Pazzaglia, F. J., & Brandon, M. T. (2001). A fluvial record of long-term steady-state uplift and erosion across the Cascadia forearc high, western Washington state. *American Journal of Science*, 301(4–5), 385–431.

Pichot, T., & Nalpas, T. (2009). Influence of synkinematic sedimentation in a thrust system with two decollement levels; analogue modelling. *Tectonophysics*, 473(3–4), 466–475.

Ramos, V. A., & Folguera, A. (2009). Andean flat-slab subduction through time. *Geological Society, London, Special Publications*, 327(1), 31–54.

Ranalli, G. (1995). *Rheology of the earth* (2nd ed., p. 413). Chapman and Hall.

Reiners, P. W., Ehlers, T. A., & Zeitler, P. K. (2005). Past, present, and future of thermochronology. *Reviews in Mineralogy and Geochemistry*, 58(1), 1–18.

Ruh, J. B., Gerya, T., & Burg, J. P. (2013). High-resolution 3D numerical modeling of thrust wedges: Influence of décollement strength on transfer zones. *Geochemistry, Geophysics, Geosystems*, 14(4), 1131–1155.

Ruh, J. B., Kaus, B. J., & Burg, J. P. (2012). Numerical investigation of deformation mechanics in fold-and-thrust belts: Influence of rheology of single and multiple décollements. *Tectonics*, 31(3), TC3005.

Schellart, W. P., Freeman, J., Stegman, D. R., Moresi, L., & May, D. (2007). Evolution and diversity of subduction zones controlled by slab width. *Nature, 446*(7133), 308–311.

Schmid, M., Ehlers, T. A., Werner, C., Hickler, T., & Fuentes-Espoz, J. P. (2018). Effect of changing vegetation and precipitation on denudation – Part 2: Predicted landscape response to transient climate and vegetation cover over millennial to million-year timescales. *Earth Surface Dynamics, 6*(4), 859–881.

Sharma, H., Ehlers, T. A., Glotzbach, C., Schmid, M., & Tielbörger, K. (2021). Effect of rock uplift and Milankovitch timescale variations in precipitation and vegetation cover on catchment erosion rates. *Earth Surface Dynamics, 9*(4), 1045–1072.

Sommaruga, A. (1999). Décollement tectonics in the Jura foreland fold-and-thrust belt. *Marine and Petroleum Geology, 16*(2), 111–134.

Starke, J., Ehlers, T. A., & Schaller, M. (2020). Latitudinal effect of vegetation on erosion rates identified along western South America. *Science, 367*(6484), 1358–1361.

Sternai, P. (2020). Surface processes forcing on extensional rock melting. *Scientific Reports, 10*, 1–13.

Stewart, R. J., Hallet, B., Zeitler, P. K., Malloy, M. A., Allen, C. M., & Trippett, D. (2008). Brahmaputra sediment flux dominated by highly localized rapid erosion from the easternmost Himalaya. *Geology, 36*(9), 711–714.

Tang, L., Yang, K., Jin, W., Lü, Z., & Yu, Y. (2008). Multi-level decollement zones and detachment deformation of Longmenshan thrust belt, Sichuan Basin, Southwest China. *Science in China Series D: Earth Sciences, 51*(2), 32–43.

Thieulot, C., Fullsack, P., & Braun, J. (2008). Adaptive octree-based finite element analysis of two-and three-dimensional indentation problems. *Journal of Geophysical Research: Solid Earth, 113*(B12), B12207.

Thieulot, C., Steer, P., & Huismans, R. S. (2014). Three-dimensional numerical simulations of crustal systems undergoing orogeny and subjected to surface processes. *Geochemistry, Geophysics, Geosystems, 15*(12), 4936–4957.

Ueda, K., Willett, S. D., Gerya, T., & Ruh, J. (2015). Geomorphological-thermo-mechanical modeling: Application to orogenic wedge dynamics. *Tectonophysics, 659*, 12–30.

Van Balen, R. T., Van der Beek, P. A., & Cloetingh, S. A. P. L. (1995). The effect of rift shoulder erosion on stratal patterns at passive margins: Implications for sequence stratigraphy. *Earth and Planetary Science Letters, 134*(3–4), 527–544.

Vauchez, A., Tommasi, A., & Mainprice, D. (2012). Faults (shear zones) in the Earth's mantle. *Tectonophysics, 558*, 1–27.

Vogt, K., Matenco, L., & Cloetingh, S. (2017). Crustal mechanics control the geometry of mountain belts. Insights from numerical modelling. *Earth and Planetary Science Letters, 460*, 12–21.

Whipp, D. M., Ehlers, T. A., Braun, J., & Spath, C. D. (2009). Effects of exhumation kinematics and topographic evolution on detrital thermochronometer data. *Journal of Geophysical Research: Earth Surface, 114*(F4), F04021.

Whipple, K. X. (2004). Bedrock rivers and the geomorphology of active orogens. *Annual Reviews Earth and Planetary Sciences, 32*, 151–185.

Willett, S., Beaumont, C., & Fullsack, P. (1993). Mechanical model for the tectonics of doubly vergent compressional orogens. *Geology, 21*(4), 371–374.

Zeitler, P. K., Meltzer, A. S., Brown, L., Kidd, W. S., Lim, C., & Enkelmann, E. (2014). Tectonics and topographic evolution of Namche Barwa and the easternmost Lhasa block, Tibet. In *Toward an improved understanding of uplift mechanisms and the elevation history of the Tibetan plateau* (Vol. *507*, pp. 23–58). Geological Society of America Special Papers.

Zeitler, P. K., Meltzer, A. S., Koons, P. O., Craw, D., Hallet, B., Chamberlain, C. P., Kidd, W. S. F., Park, S. K., Seeber, L., Bishop, M., & Shroder, J. (2001). Erosion, Himalayan geodynamics, and the geomorphology of metamorphism. *GSA Today, 11*(1), 4–9.

## SUPPORTING INFORMATION

Additional supporting information may be found in the online version of the article at the publisher's website.